WPRM-PR(18) 21300

S Grazioso et al.

Multibody Simulations of the Telescopic Articulated Remote Manipulator with Flexible Payload for DEMO Studies on Remote Handling

Preprint of Paper to be submitted for publication in
Fusion Engineering and Design

This work has been carried out within the framework of the EUROfusion Consortium and has received funding from the Euratom research and training programme 2014-2018 under grant agreement No 633053. The views and opinions expressed herein do not necessarily reflect those of the European Commission.

Multibody Simulations of the Telescopic Articulated Remote Manipulator with Flexible Payload for DEMO Studies on Remote Handling

Stanislao Grazioso[a,*], Roger Powell[b], Robert Skilton[b], Giuseppe Di Gironimo[a], Bruno Siciliano[a]

[a] *CREATE/University of Naples Federico II, P.le Tecchio 80, 80125 Napoli, Italy*
[b] *RACE/UKAEA, Culham Science Centre, Abingdon, Oxfordshire OX14 3DB, UK*

Abstract

This paper presents the multibody simulations of a coupled flexible mechanical system intended to be used for DEMO studies on remote handling. The system comprises a very large kinematically redundant spatial manipulator onto which is attached a flexible payload as a test bench for the blanket control problem. The system model is based on a novel screw–based finite element formulation built on top of geometrically exact beam theory and flexible multibody dynamics. The results show that payload flexibility must be taken into account, even for slow systems such as remote handling equipment, in order to accomplish safe operations.

Keywords:

1. Introduction

DEMO remote maintenance tasks will require manoeuvring extreme loads with long–reach robotic manipulators [1]. One of the major examples is the installation/replacement of DEMO blanket multi–segment modules (MMS) using articulated mechanisms [2].
In nuclear fusion reactors, remote handling of in–vessel components generates undesired vibrations: therefore, in the last years a lot of effort has put on studying the effects of flexibility in motion control of DEMO remote handling equipment. To this end, RACE/CCFE has recently installed the telescopic articulated remote manipulator (*TARM*), one of the three large articulated booms used in the JET remote maintenance system. This experimental system will facilitate the design, testing and performance evaluation of adaptive position control systems (APCS) for DEMO remote maintenance [3]. In order to study the motion control of a fluid–like flexible payload that could approximate to a MMS, a *flexible payload* has been designed and manufactured to be attached to the last flange of TARM [4].
Recent approaches use artificial neural networks for modeling large flexible machines for DEMO remote maintenance [5, 6].
Differently, our strategy in this context is based on physical modeling [7]. In this paper, we present the multibody modeling and simulations of the TARM with flexible payload, using the simulator developed during the FlexARM project [1]. In Sec. 2 we present the mechanical design of the system, while in Sec. 3 the modeling strategy, assumptions and dynamic parameters used in this study. Section 4 presents simulation results, with conclusions given in Sec. 5.

*Corresponding author.
Email address: stanislao.grazioso@unina.it (Stanislao Grazioso)

[1] FlexARM project

2. Design description

The CAD models of the TARM with flexible payload are illustrated in Fig. 1. From one side, the TARM system is rigidly attached to a supporting steel frame; from the other side, it can be coupled with tools and/or end–effectors: in this study, it is attached to the flexible payload.

The TARM system [8] comprises a vertical telescopic mast (from now on, axis B2), held in place by the vertical telescope guide, which is attached to the support frame. The lower end of the telescopic mast is a rotary flange unit (from now on, axis B3) to which the horizontal boom is directly attached. The first joint, located below B3, is a revolute pitch joint (known as A1). This also houses the second joint, known as A2, which provides a horizontal prismatic movement of 3.8 m. Attached to A2 is a sequence of yaw joints, known as A3, A3b and A4, which are all revolute in the vertical axis. The joint A3b together with the rigid links to A3 and A4, respectively, is a composite piece known as the Boom Addition, that can be removed if desired. The Boom Addition provides an additional 2 m of reach. The next section, known as the Boom Extension, is attached to the A4 (yaw) joint and comprises two revolute joints A5 (pitch) and A6 (roll), respectively. The Boom Extension can be connected either directly to A3 or to the Boom Addition. In this work, it is assumed that the Boom Addition is used.

A flexible payload [4] is rigidly mounted to a flange on the roll joint A6 at the end of the Boom Extension. The flexible load comprises both active and passive parts. The active payload is made up by a guided linear servo motor which accelerates a rigid mass in a direction parallel to the pitch axis of A5. This system can be used to study dynamic disturbances to the TARM system. The passive part comprises a slender vertical plate to which additional masses can be attached, there is also a coupling such that the active system can excite the passive system. These systems will be used in the development and fine-tuning of the APCS.

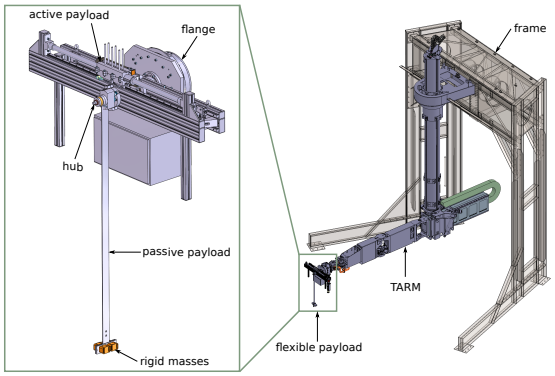

Figure 1: CAD models of TARM with flexible payload

3. Multibody dynamic model

The multibody dynamic model is based on a recent screw–based finite element formulation for flexible mechanical systems [9]. The same approach was used to derive the dynamic model of the hybrid kinematic mechanism for DEMO blanket remote handling [10]. In this section we first present the equations of motion of a generic manipulator; then, we describe the elements of the TARM model and flexible payload.

3.1. Equations of motion

TARM with flexible payload is a generic flexible mechanical system where the manipulator is composed by rigid links connected through kinematic joints, where the payload is considered to be flexible. The effects of the joints connecting the bodies could be taken into account by imposing a set of algebraic constraints, which prevent the non–allowed motion as imposed by the joint. A single rigid body is described by the motion of one node in its center of gravity, to which a frame $\boldsymbol{H}_{CoG} \in SE(3)$ is attached; a flexible body is described by the motion of two extreme nodes, to which two frames $\boldsymbol{H}_A \in SE(3)$ and $\boldsymbol{H}_B \in SE(3)$ are attached and connected through an helical shape function [11]. Indeed, the relative motion between two nodes 1 and 2, belonging to two different bodies, can be described by a relative frame $\boldsymbol{H}_{J,I} \in$ Lie subgroup of SE(3) as $\boldsymbol{H}_2 = \boldsymbol{H}_1\boldsymbol{H}_{J,I}$. Collecting the motion variables in the matrix $\boldsymbol{H} = \text{diag}(\boldsymbol{H}_1, \ldots, \boldsymbol{H}_n, \boldsymbol{H}_{J,1}, \ldots, \boldsymbol{H}_{J,k})$, with n the number of nodes and k the number of joints of the system, the strong form for the global dynamic equilibrium of the system take the form

$$\boldsymbol{M}(\boldsymbol{H})\dot{\boldsymbol{\eta}} - \boldsymbol{C}(\boldsymbol{H})\boldsymbol{\eta} + \boldsymbol{f}_{int}(\boldsymbol{H}) + \boldsymbol{f}_{\varphi}(\boldsymbol{H}, \boldsymbol{\lambda}) = \boldsymbol{f}_{ext}(\boldsymbol{H}) \tag{1}$$

where $\boldsymbol{\eta}$ contains the absolute and relative velocities of the nodes and joints of the system, $\boldsymbol{M}$ and $\boldsymbol{C}$ are the global discretized mass and velocity matrices; $\boldsymbol{f}_{int}$ are the discretized global internal forces, including elastic forces of the beams and elastic and dissipative forces of the flexible joints; $\boldsymbol{f}_{\varphi}$ are the discretized constraint forces, with $\boldsymbol{\lambda}$ the Lagrange multiplier vector; $\boldsymbol{f}_{ext}$ are the discretized global external forces, including also gravity. An algebraic constraint equation $\boldsymbol{\varphi}(\boldsymbol{H}) = \boldsymbol{0}$ must be appened to the differential system (1) to define a differential-algebraic equation (DAE) system that must be solved for $(\boldsymbol{H}, \boldsymbol{\lambda})$. Finally, a geometric implicit integration scheme and a Newton-Raphson iterative method can be conveniently used to numerically solve the DAE system [12].

3.2. Description of the model

The schematic model of the TARM with flexible payload is illustrated in Fig. 2a, with the geometric data given in Fig. 2b, as taken from the reference CAD models. The connection point between the longitudinal axis of the vertical telescope guide and the mast column's axis has been selected as the origin of the reference frame.

The bodies of the TARM have been modeled using rigid elements, since the cross–sections of the elements make the links very stiff: this was proved in simulations in [13] and in experimental tests made at CCFE/RACE. Therefore, the TARM model comprises 16 rigid links (14 rigid links as in [14] plus one rigid link for the vertical telescope guide and one for the mast column), 9 kinematic joints with 1 DoF (2 prismatic and 7 revolute), 6 rigid constraints and one clamped element (the vertical telescope guide). Each rigid element adds 6 DoF; each joint removes 5 DoF; each rigid constraint removes 6 DoF; each clamped boundary condition removes 6 DoF. Hence, the TARM has a total of 9 DoF ($+16 \cdot 6 - 9 \cdot 5 - 6 \cdot 6 - 1 \cdot 6 = 9$). The frame to support the TARM is added as well, and it has been modeled as a rigid element.

In this paper we will study the effects of the passive part of the payload: therefore, the part of the payload from the flange to the vertical slender plate has been modeled as a rigid element, while the passive part has been modeled as a nonlinear beam element with an attached rigid mass.

Table 1 reports the center of gravity, the mass and the rotational inertia of each rigid body involved in the model. The inertia properties of the rigid bodies (mass and rotational inertia) have been estimated from the CAD models, or, when available, taken from [14]. Notice that for some bodies the rotational inertia is not indicated: this means that we were not able to estimate it from the available CAD models (i.e. empty models, no material properties); in this case we just consider lumped masses.

The joint definition and their maximum velocity are reported in Table 2. The joint maximum velocities have been taken from [15], when available. The only assumed velocities are: A1 (1/10 of B3) and A5, A6 (1/5 of B3).

The flexible part of the payload is an aluminum rectangular plate with length $l = 1.585\,\text{m}$ and cross-

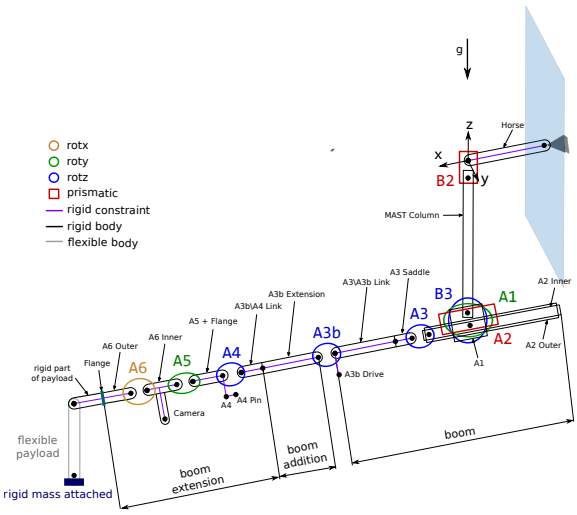

(a) Description of the elements

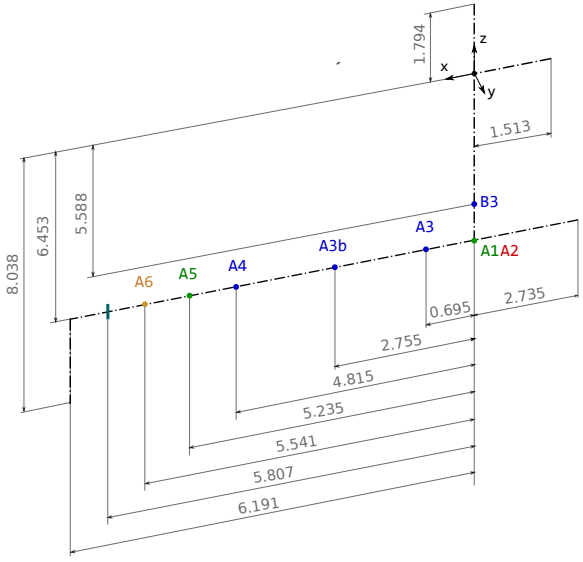

(b) Geometric data. Measurements in [m]

Figure 2: Model of TARM with flexible payload

section dimensions $b = 0.050\,\mathrm{m}$ and $h = 0.005\,\mathrm{m}$. Since one dimension is dominant, we model it using beam elements. In particular, we use a finite strain geometrically exact beam model involving all the components of deformations (axial, shear, bending, torsion) [16]. Table 3 reports the cross-section and material properties of the flexible payload. Notice that in this table the shear corrector factors k_x and k_y for shear areas of rectangular sections are reported, together with the torsion corrector factor k_J. These are important for correcting the shear stiffnesses and torsional stiffness of generic cross-sections. Since the payload is initially parallel to the z-axis (i.e vertical), the mass and stiffness matrices of the cross-section are diagonal. The mass matrix is given by $\mathbf{M} = \mathrm{diag}(\rho A, \rho A, \rho A, \rho I_x, \rho I_y, \rho J)$, being ρA the mass per unit length, I_x and I_y the moment of inertia and J the polar moment of inertia. Indeed, the stiffness matrix is given by $\mathbf{K} = \mathrm{diag}(GA_x, GA_y, EA, EI_x, EI_y, GJ)$, being GA_x and GA_y the shear stiffnesses, EA the axial stiffness, EI_x and EI_y the bending stiffnesses and GJ the torsional stiffness.

Table 1: Positions and inertia properties in principal axes of the rigid bodies (position in [m]; mass in [kg]; rotation inertia in [kgm^2])

rigid body	CoG (x, y, z)	m [kg]	J_{xx}	J_{yy}	J_{zz}
Support frame	–	2000	–	–	–
Vertical telescope guide	–	600	–	–	–
Mast column	–	600	–	–	–
A1	(-0.2634,0,-6.453)	498.3	–	–	–
A2 Outer	(-1.228,0,-6.453)	807.1	120.887	737.179	667.858
A2 Inner	(-0.955,0,-6.453)	447.1	39.282	477.411	448.426
A3 Saddle	(-0.982,0,-6.453)	63.01	6.689	6.948	1.401
A3/A3b Link	(2.01,0,-6.453)	78.57	8.546	30.575	24.574
A3b Drive	(2.79,0,-6.453)	53.43	0.639	1.362	1.461
A3b Extension	(3.30,0,-6.453)	54.96	5.153	13.195	9.482
A3b/A4 Link	(4.35,0,-6.453)	65.1	8.546	30.575	24.574
A4	(4.85,0,-6.453)	21.06	0.159	1.64	0.221
A4 Pin	(5.03,0,-6.453)	5.03	0.015	0.016	0.005
A5 + Flange	(5.2113,0,-6.453)	60.84	1.132	2.176	1.569
A6 Inner	(5.47,0,-6.453)	32.45	0.629	1.063	0.889
Camera	(5.5154,0,-7.054)	12.62	0.997	0.993	0.025
A6 Outer	(5.7,0,-6.453)	52.13	1.989	1.436	0.867
Payload (rigid)	(6.052,0,-6.453)	62	–	–	–

Table 2: Kinematic joint definition (P = prismatic; R = revolute) and their maximum velocity (P: [ms^{-1}]; R: [rads^{-1}]).

joint	DoF	joint type	joint axis	$v_{\max}$
B2	1	P	z	0.050
B3	1	R	z	0.062
A1	1	R	y	0.0062
A2	1	P	x	0.046
A3	1	R	z	0.116
A3b	1	R	z	0.052
A4	1	R	z	0.062
A5	1	R	y	0.0124
A6	1	R	x	0.0124

Table 3: Cross-section and material properties of the flexible payload. b = base; h = height; A = area; k_x, k_y = shear corrector factors; A_x, A_y = shear area; k_J = torsion corrector factor; I_x, I_y = second moment of inertia of the cross-section; J = torsion constant; ρ = density; E = Young modulus; ν = Poisson ratio; G = Shear modulus.

b	$0.050\,\mathrm{m}$
h	$0.005\,\mathrm{m}$
A	$b \cdot h$
k_x	0.8333
k_y	0.5909
A_x	$k_x \cdot A$
A_y	$k_y \cdot A$
k_J	$1/(3 + 4.1 \cdot (b/h)^{3/2})$
I_x	$h \cdot b^3/12$
I_y	$b \cdot h^3/12$
J	$k_J \cdot h \cdot b^3$
ρ	$2700\,\mathrm{kgm}^{-3}$
E	$69 \times 10^9\,\mathrm{Nm}^{-2}$
ν	0.3
G	$E/(2(1+\nu))$

4. Simulations

The simulations were performed using the FlexARM simulator [7], which can be used for rigid/flexible multibody systems articulated in generically complex topological structures and connected to rigid/flexible payloads.

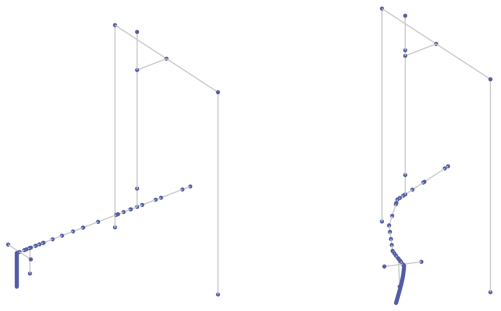

(a) t = 0 s (b) t = 10 s

Figure 3: Snapshots of TARM with flexible payload (images from the FlexARM simulator).

4.1. Simulation 1: simultaneous actuation

Simulation 1 shows the motion of the TARM when all its nine joints are actuated simultaneously, with point-to-point *bang-bang acceleration profiles*, at their maximum velocities. This profile imposes a constant acceleration in the start phase and a constant deceleration in the arrival phase (triangular profiles for the velocities and $S-$shaped profile for the positions). The actuation holds for 10 s, while the motion is observed for 20 s. Figure 3a shows a snapshot of the TARM at t = 0 s, where Fig. 3b at t = 10 s. The maximum joint velocities are taken from Table 2; for an $S-$shaped profile, the final position of each joint q_f is calculated as $q_f = v_{max} \cdot t_f/2$, with $t_f = 10$ s, while the acceleration as $\ddot{q} = 4(q_f - q_i)/t_f^2$. The input trajectories can be directly computed from the values of position and acceleration of Table 4; thus, they are not plotted here. Figure 4 shows directly the outputs in terms of x, y and z displacements of the CoG of the six main elements of the TARM (see legend of Fig. 4 and Table 1 for the initial positions).

In order to show the effects of payload flexibility, we performed Simulation 1 again, forcing the payload to behave as a rigid aluminum plate. Figure 5 shows the trajectories described by the tip of the payload, with the two modeling assumptions: rigid and flexible aluminum plate. As we can expect, the two trajectories differ and their difference increases from the start to the end of the simulation. Let $T_R = (x_R, y_R, z_R)$ be the position of the payload tip with the rigid assumption and $T_F = (x_F, y_F, z_F)$ be the position of the payload tip with the flexible assumption, we define a distance measure $d(T_R - T_F) = d$ between the two tip trajectories as

$$d = \sqrt{(x_R - x_F)^2 + (y_R - y_F)^2 + (z_R - z_F)^2} \quad (2)$$

which is plotted in Fig. 6. The distance measure increases for 10 s from 0 to around 0.16 m; after which it oscillates about this average value until the end of the simulation (20 s).

Table 4: Joint point-to-point motions with S profiles for Simulation 1. q_i: initial position; q_f: final position (P: [m]; R: [rad]). $\ddot{q}$: acceleration (P: [ms^{-2}]; R: [rads^{-2}])

Joint	B2	B3	A1	A2	A3	A3b	A4	A5	A6
q_i	0	0	0	0	0	0	0	0	0
q_f	0.250	0.31	0.031	0.230	0.58	0.26	0.31	0.062	0.062
$\ddot{q}$	0.01	0.0124	0.00124	0.0092	0.0232	0.0104	0.0124	0.00248	0.00248

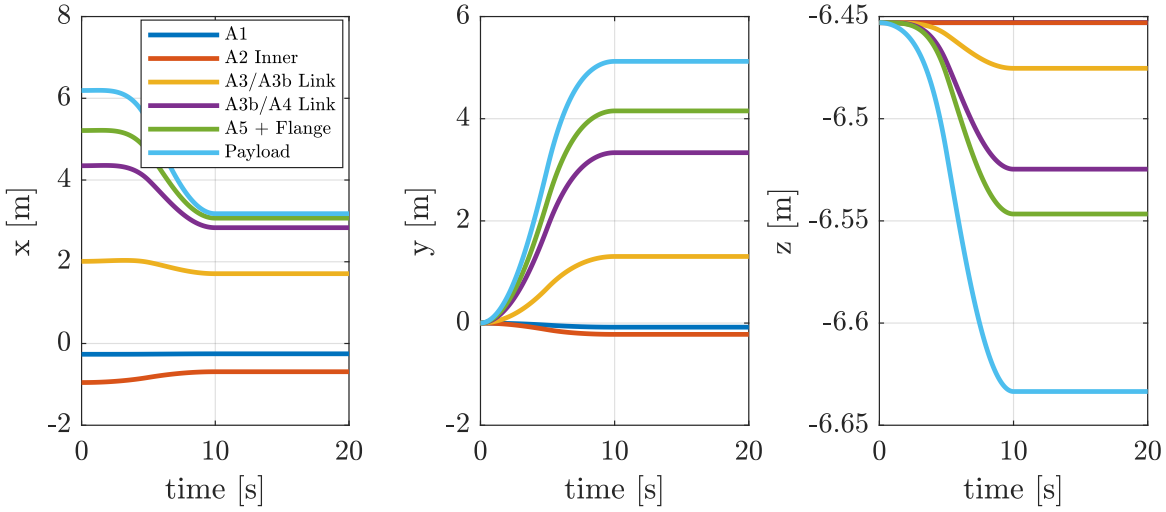

Figure 4: Outputs of Simulation: three-dimensional displacements of the six main elements of the TARM.

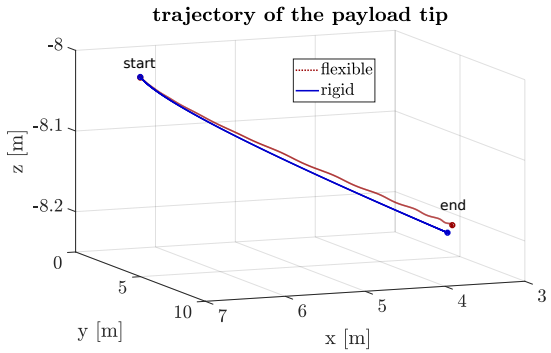

Figure 5: Trajectory of the tip of the payload for the overall duration of the Simulation.

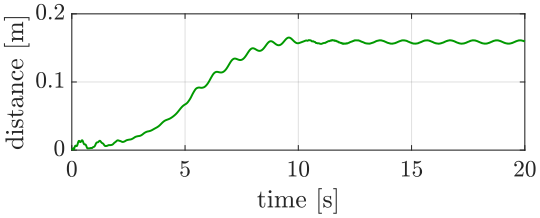

Figure 6: Distance measure between the tip trajectories defined by the rigid and flexible models.

4.2. Simulation 2: consecutive actuation

Simulation 2 considers the consecutive actuation of the nine joints: each joint actuates for 10 s, thus the total duration of the simulation is 90 s. Figure 7 shows the input trajectories of the joints: when they are actuated (for 10 s), they follow a *trapezoidal velocity profile*. This motion profile imposes a constant acceleration in the start phase, a cruise velocity, and a constant deceleration in the arrival phase. The resulting trajectory is formed by a linear segment connected by two parabolic segments to the initial and final positions. The final positions for each joint are the same q_f values reported in Table 4, and, once reached by the joint, they are kept constant for the remaining part of the simulation. The first phase (constant acceleration), second phase (cruise velocity) and third phase (constant deceleration) of the trajectory last respectively 2.5 s, 5 s and 2.5 s. The resulting position trajectory is different from the $S-$shaped one, which can be seen as a particular case of trapezoidal velocity profile where the second phase (the one at cruise velocity) lasts 0 s. The difference between the triangular velocity profile and the trapezoidal velocity profile is that the latter, for equal final position q_f, allows reducing the maximum velocity. Indeed, with the combination of three phases used in this simulation (0.25;0.50;0.25), we have that $v_{max,trapezoidal} = 3/4 \cdot v_{max,triangular}$.
Figure 8 shows the output of Simulation 2, namely, the three components of displacements for the six main elements of the TARM. As done before, we plot the trajectory of the payload tip, once assuming the aluminum plate to be rigid, once assuming it to be flexible (see Fig. 9) Again, we notice a difference in the trajectories mainly in the final part. As we can see from Fig. 10, the distance measure (computed using Eq. 2) when all joints reach their final values q_f is approximately the same as Simulation 1 (around 0.16 m). However, there are two great raises: the first one from almost 0 m to 0.05 m in the temporal range 20 s to 30 s and the second from around 0.05 m to 0.15 m in the temporal range 70 s to 80 s. These two raises correspond respectively to the motion caused by A1 and A5 joints: the motion about $y-$ axis is the main source of flexible behaviors, thus movements about this axis should be minimized. Another movement which induces a major source of flexibility is the one in the last part of the trajectory (movements about $x-$axis, from 80 s to 90 s). Indeed, movements about $z-$ axis produces mainly oscillations around the same average value of distance.

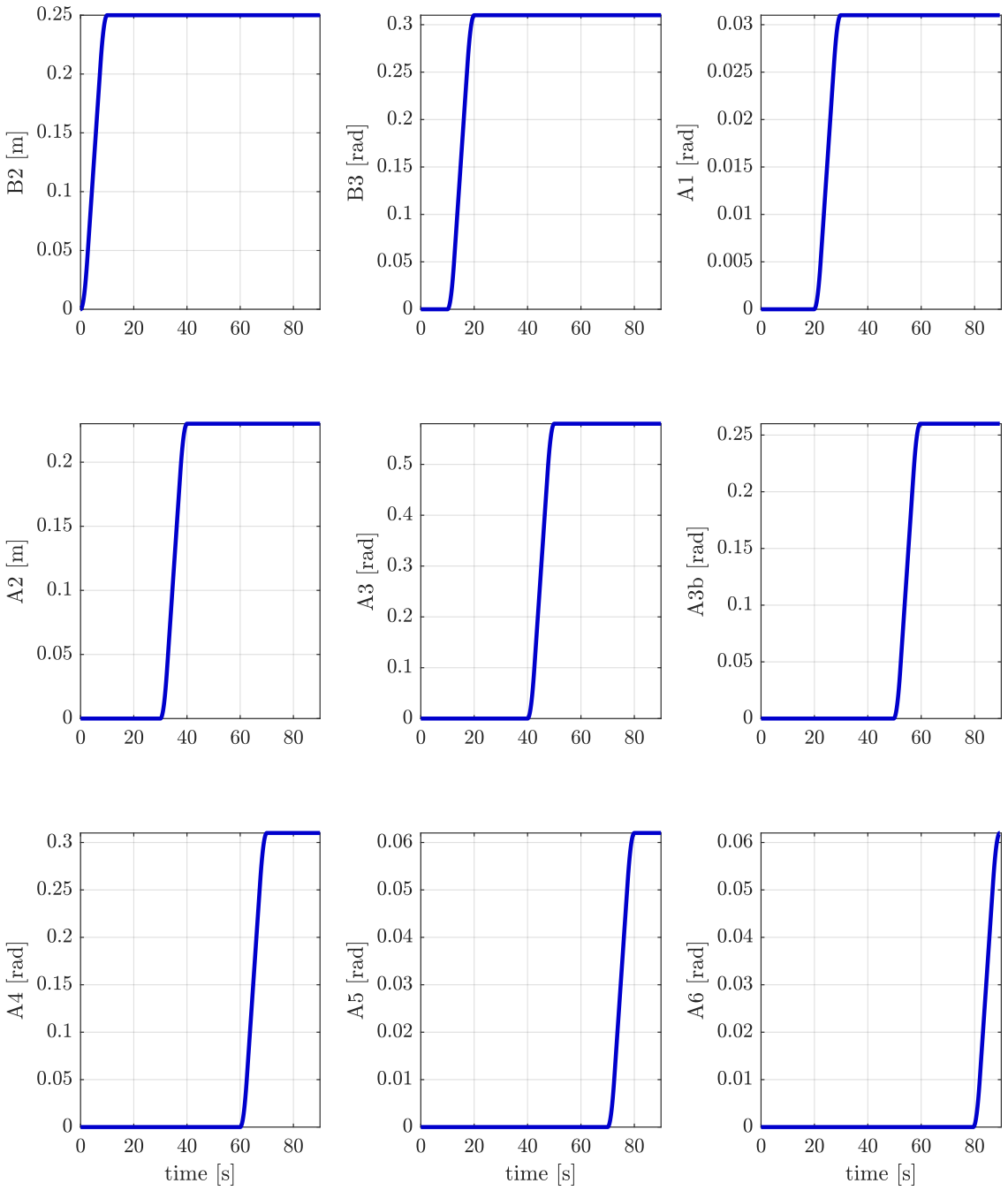

Figure 7: Input joint trajectories for Simulation 2.

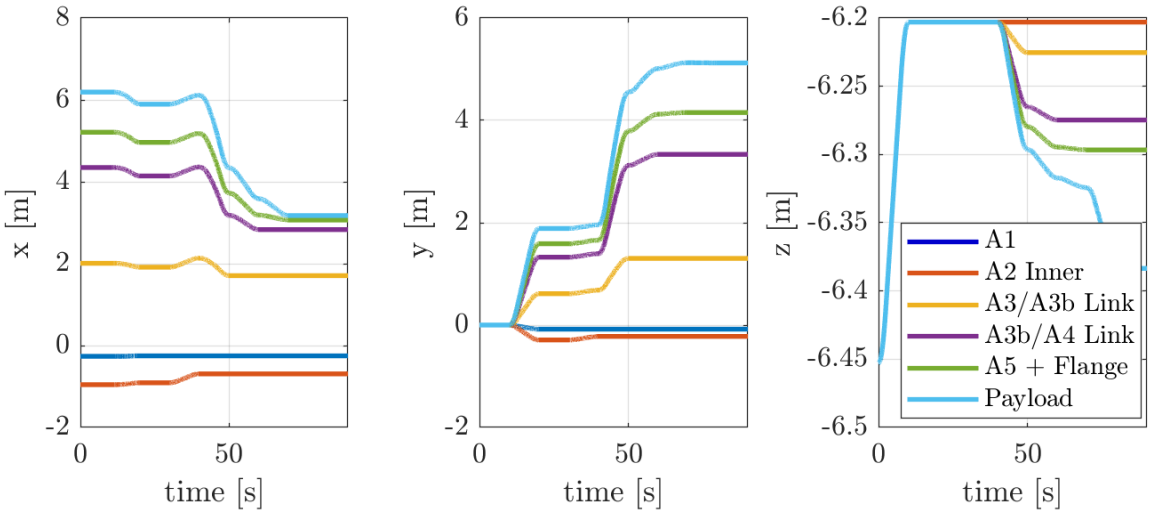

Figure 8: Outputs of Simulation 2: three-dimensional displacements of the six main elements of the TARM.

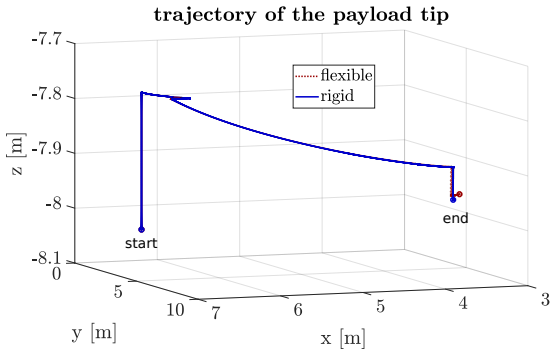

Figure 9: Trajectory of the tip of the payload for the overall duration of the Simulation 2.

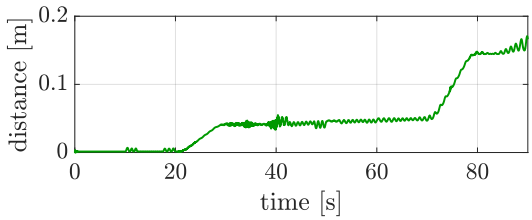

Figure 10: Trajectory of the tip of the payload

5. Conclusions

In this paper we presented the dynamic modeling and simulation of the TARM with a flexible payload. The system model is based on a novel screw–based finite element formulation for flexible mechanical systems. We started by describing the mechanical design of the system. Then, we described the system model in terms of rigid and flexible bodies, joints, constraints and boundary conditions. The simulations consider the manipulator to be rigid and the payload to be flexible. Even for the very slow motion typical of remote handling equipment, the use of rigid payload models gives an approximation ($\sim 0.2\,\mathrm{m}$) which is unacceptable for manoeuvring components in tiny spaces as tokamak machines.
Predictive models can provide a great insight into manipulator–payload behavior and interactions: therefore, they are a prerequisite for design of control systems for remote handling equipment in challenging domains as DEMO.

Acknowledgements

This work has been carried out within the framework of the EUROfusion Consortium and has received funding from the Euratom research and training program 2014-2018 under grant agreement No 633053. The views and options expressed herein do not necessarily reflect those of the European Commision.

References

[1] O. Crofts, A. Loving, D. Iglesias, M. Coleman, M. Siuko, M. Mittwollen, V. Queral, A. Vale, E. Villedieu, Overview of progress on the european demo remote maintenance strategy, Fusion Engineering and Design 109 (2016) 1392–1398.

[2] J. Keep, S. Wood, N. Gupta, M. Coleman, A. Loving, Remote handling of demo breeder blanket segments: Blanket transporter conceptual studies, Fusion Engineering and Design 124 (2017) 420–425.

[3] R. Skilton, Adaptive position control system development, Report reference, RACE (2018).

[4] O. Caretta, Functional and technical specifications for apcs payload, Report reference, RACE (2017).

[5] M. Li, H. Wu, H. Handroos, Y. Wang, A. Loving, O. Crofts, M. Coleman, R. Skilton, G. Burroughes, J. Keep, et al., Dynamic model identification method of manipulators for inside demo engineering, Fusion Engineering and Design 124 (2017) 638–644.

[6] M. Li, H. Wu, H. Handroos, R. Skilton, J. Keep, A. Loving, Comparison of deformation models of flexible manipulator joints for use in demo, IEEE Transactions on Plasma Science 46 (5) (2018) 1198–1204.

[7] S. Grazioso, G. Di Gironimo, B. Siciliano, Modeling and vibration control of flexible mechanical systems for demo remote maintenance: results from the flexarm project, Fusion Engineering and Design (2018) submitted.

[8] Tarm maintenance manual, Tech. rep., Joint European Torus.

[9] S. Grazioso, V. Sonneville, G. Di Gironimo, O. Bauchau, B. Siciliano, A nonlinear finite element formalism for modelling flexible and soft manipulators, in: IEEE International Conference on Simulation, Modeling, and Programming for Autonomous Robots (SIMPAR), IEEE, 2016, pp. 185–190.

[10] S. Grazioso, G. Di Gironimo, D. Iglesias, B. Siciliano, Screw-based dynamics of a serial/parallel flexible manipulator for demo blanket remote handling, Fusion Engineering and Design (2018) to be appeared.

[11] S. Grazioso, G. Di Gironimo, B. Siciliano, From differential geometry of curves to helical kinematics of continuum robots using exponential mapping, in: International Symposium on Advances in Robot Kinematics, Springer, 2018, pp. 319–326.

[12] O. Brüls, A. Cardona, M. Arnold, Lie group generalized-α time integration of constrained flexible multibody systems, Mechanism and Machine Theory 48 (2012) 121–137.

[13] S. Grazioso, Dynamic modeling and simulation of the telescopic articulated remote mast with flexible payload, Tech. rep., RACE/CCFE (2018).

[14] R. Powell, Actuator forces, Report reference, RACE (2018).

[15] Technical description of tarm joints, Tech. rep., Joint European Torus.

[16] S. Grazioso, G. Di Gironimo, B. Siciliano, A geometrically exact model for soft continuum robots: the finite element deformation space formulation, Soft Robotics (2018) to be appeared.